

# School of Physics



## Senior Honors Project Physics 4

# Quantum Physics: Illusion or Reality?

*Conor Fitzpatrick*<sup>1</sup> & Iain McMichael  
December 6, 2006

### Abstract

The relative linear polarisation of  $\gamma$  ray photons emitted with opposite parity from the annihilation of positronium produced by the decay of  $^{22}\text{Na}$  was measured by way of Compton polarimetry using two-fold coincidence counting techniques. The results are in good agreement with quantum-mechanical calculations. This has implications for any *local* hidden variables theory as proposed by Einstein *et al*[1]. As yet, no satisfactory hidden variables theories in which locality may be violated have been proposed. We therefore conclude it is likely that Quantum Mechanics is a complete theory.

### Declaration

I declare that this project and report is my own work.

Signature:

**Supervisors:** Dr. T. Davinson, Prof. P. Woods

Date: December 6, 2006

6 Weeks

---

<sup>1</sup>Author email: s0127440@sms.ed.ac.uk

# Contents

<b>1</b>	<b>Introduction</b>	<b>2</b>
<b>2</b>	<b>Theory</b>	<b>2</b>
2.1	Quantum-Mechanical Wavefunction . . . . .	3
2.2	Local Hidden Variables Wavefunction . . . . .	3
2.3	The application of Compton Polarimetry to the measurement of polarisation of $\gamma$ s . . . . .	3
2.3.1	Further Manipulation of The Quantum Mechanical Wavefunction	4
2.3.2	Further Manipulation of the Local Hidden Variables Wavefunction	4
<b>3</b>	<b>Method</b>	<b>4</b>
3.1	Mechanical considerations . . . . .	4
3.2	Electronics . . . . .	5
3.3	Optimisation of Acquisition times . . . . .	5
3.4	Error minimisation . . . . .	6
<b>4</b>	<b>Results</b>	<b>7</b>
<b>5</b>	<b>Conclusion</b>	<b>9</b>
<b>6</b>	<b>Appendices</b>	<b>11</b>
<b>A</b>	<b>Compton Polarimetry</b>	<b>12</b>
<b>B</b>	<b>modelling</b>	<b>13</b>
B.1	Simple model and derivation of relative intensities . . . . .	13
B.1.1	Quantum model . . . . .	13
B.1.2	Local Hidden Variables Model . . . . .	14
B.2	Further modelling . . . . .	15
B.2.1	Compton angle specification . . . . .	15
B.2.2	Polarisation angle specification . . . . .	16
<b>C</b>	<b>Detector Calibration &amp; Configuration</b>	<b>16</b>
C.1	Channel-Energy determination . . . . .	17
C.2	Timing calibration . . . . .	18
C.3	Energy coincidence criteria . . . . .	20
<b>D</b>	<b>Error and acquisition time optimisation</b>	<b>22</b>

# 1 Introduction

In 1935, Albert Einstein, Boris Podolski and Nathan Rosen published a paper[1] commonly referred to as the *EPR Paradox*. This paper brought into question the “*completeness*” of Quantum Mechanics, and proposed that a complete solution relied upon having “*physical reality*”<sup>2</sup> in order to satisfy classical intuitions such as the principle of locality. Einstein in particular struggled with the concept of non-commutative observables having simultaneous reality as this appeared to violate his own well understood theories of relativity. John Bell (and later others) formalised this philosophical argument in the form of inequalities[2], in the hope that they may be tested by experiment. This report discusses one such experiment.

The original thought experiment proposed in the EPR paper was a generalised application of Quantum Mechanics, consisting of two entangled systems sufficiently separated so that they no longer interact, with physical quantities (*observables*)  $A$  and  $B$ . The Bell paper applies this to a pair of spin  $\frac{1}{2}$  particles initially formed in the spin-singlet state, and considers measurement of the spin by way of the Stern-Gerlach method. In this report we consider the same application to a somewhat more practical experiment. Sources of correlated photons with correlated polarisations are readily available in the form of radioisotopes that decay by way of  $\beta^+$  emission. Such entangled photon pairs satisfy the same locality requirements as proposed by Einstein *et al.* in their original paper.

## 2 Theory

We consider first the annihilation of positronium.

$$e^+ + e^- |_{[l=0,s=0]} \rightarrow \gamma\gamma |_{[m=\pm 1]} \quad (1)$$

Not considered here is the  $s = 1$  state, which decays to three  $\gamma$ s.

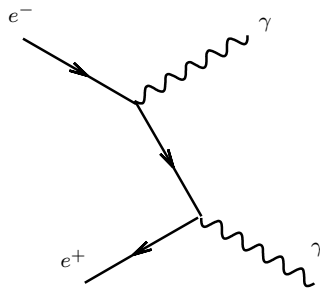


Figure 1: First order Feynman Vertex diagram of electron-positron annihilation. The electron emits a real  $\gamma$  and interacts with the positron by way of a virtual electron

The annihilation  $\gamma$ s have equal and opposite momenta, with states  $[m = 1]$ ,  $[m = -1]$  corresponding to right and left handed circularly polarised photon pairs respectively. This satisfies the requirements of the EPR thought experiment in that unless the principle of

---

<sup>2</sup>Einstein never actually referred to a “*hidden variables theory*”, but such a description is frequently used with reference to the EPR paper, and so we choose to propagate it here.

locality is violated, the photons are no longer capable of interacting. We now consider the wavefunction of this system in both the Quantum-Mechanical and Local Hidden Variables interpretations.

## 2.1 Quantum-Mechanical Wavefunction

The states  $m = 1$  and  $m = -1$  both contribute to the wavefunction. We label these states as follows:

$$\Psi_{(m=1)} = |R_1\rangle|R_2\rangle \quad (2)$$

$$\Psi_{(m=-1)} = |L_1\rangle|L_2\rangle \quad (3)$$

From parity considerations with  $\mathcal{P}(\text{motion})$  being the parity of the relative motion of the photons after annihilation,

$$\mathcal{P}\Psi = \mathcal{P}(e^+)\mathcal{P}(e^-)\mathcal{P}(\text{motion}) = -1 \quad (4)$$

as

$$\mathcal{P}(e^-) = -\mathcal{P}(e^+) \quad (5)$$

but

$$\mathcal{P}|R_1\rangle|R_2\rangle = \mathcal{P}|L_1\rangle|L_2\rangle \quad (6)$$

so the correct formulation of the wavefunction must be

$$\Psi = |R_1\rangle|R_2\rangle - |L_1\rangle|L_2\rangle \quad (7)$$

The implications of this wavefunction are straightforward. A polarisation measurement on one photon collapses the wavefunction in such a way as to define the polarisation of the other photon, but until a measurement is performed, the states are not defined.

## 2.2 Local Hidden Variables Wavefunction

The Wavefunction is composed of two independent wavefunctions, one for each photon, based upon the assumption that the initial polarisation is defined during the annihilation event.

$$\Psi = |\Psi_1\rangle|\Psi_2\rangle \quad (8)$$

So a measurement on one photon has no effect upon the measurement of the other, as both states are defined prior to measurement.

## 2.3 The application of Compton Polarimetry to the measurement of polarisation of $\gamma$ s

For a full description of the differential cross-section of a compton polarimeter and its application please refer to Appendix A. We now consider a pair of diametrically opposite compton polarimeters, centred upon a source of annihilation photons. The photons are produced with circular polarisation and the polarimeters detect linearly polarised light. We must therefore consider components of the wavefunctions:

### 2.3.1 Further Manipulation of The Quantum Mechanical Wavefunction

Taking normalised components of eq. 2 and eq. 3 with respect to an arbitrary right-handed cartesian reference frame, we find:

$$|R\rangle = \frac{1}{\sqrt{2}} (|x\rangle + i|y\rangle) \quad (9)$$

$$|L\rangle = \frac{1}{\sqrt{2}} (|x\rangle - i|y\rangle) \quad (10)$$

so substitution into eq. 7 yields:

$$\Psi = \frac{1}{2} ((|x_1\rangle + i|y_1\rangle) (|x_2\rangle + i|y_2\rangle) - (|x_1\rangle - i|y_1\rangle) (|x_2\rangle - i|y_2\rangle)) \quad (11)$$

$$\Rightarrow \Psi = i (|y_1\rangle|x_2\rangle + |x_1\rangle|y_2\rangle) \quad (12)$$

This is the final Quantum Mechanical Wavefunction considered in the report. Further modification to the Local Hidden Variables Wavefunction is trivial:

### 2.3.2 Further Manipulation of the Local Hidden Variables Wavefunction

If we consider that the polarisation angle with respect to  $\hat{x}$  is  $\phi$ , The Hidden Variables Wavefunction becomes:

$$\Psi = |\Psi_1(\phi)\rangle|\Psi_2(\phi + \frac{\pi}{2})\rangle \quad (13)$$

## 3 Method

The experimental apparatus consisted of a  $^{22}\text{Na}$  source located within a lead collimator, incident upon two diametrically opposing Perspex scatterers. Detectors consisted of two cylindrical Bicron NaI(Tl) scintillator crystals[3] mounted on Ortec Photomultiplier tubes[4]. These were free to move in the polarisation plane of the scatterers.

### 3.1 Mechanical considerations

The Pb collimator was configured in such a way as to prevent incident correlated photons having uncorrelated polarisations through scattering within the collimator itself [5]. This did however decrease the effective beam radius at the scatterer. The experiment was calibrated to ensure both detectors were centered on the source, and were diametrically opposing. This was performed using a simple laser alignment technique. Initially, concern was raised over the mechanical precision of the apparatus, but measurements of significant geometrical factors were made to within errors sufficiently small to be deemed insignificant after modelling & error considerations (< 5 %). The relative angular separation of the detectors was set using a spirit level clinometer to an accuracy of  $\pm 1^\circ$ , and was measured after acquisition at each angle to ensure mechanical stability throughout the course of the experiment.

Analytical models for increasing degrees of geometric complexity were derived using **MAPLE**. The derivation and final model may be found in Appendix B.

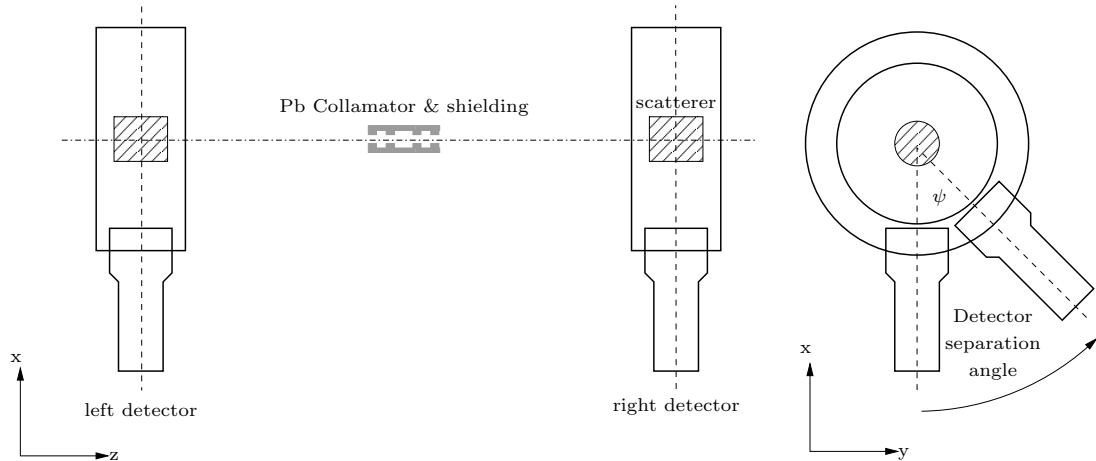


Figure 2: The experimental configuration used to measure the relative polarisation of two correlated 511keV photons.

### 3.2 Electronics

Standard NIM components were used to provide two-fold coincidence of scattered photons to within a coincidence resolving time of 550ns. Further information on the calibration and setup may be found in Appendix C. The system was tested for detector gain drift, level drift, and window drift before and after each data acquisition run. Daily measurement of lab temperature, when compared to the tolerances specified in the electronics data sheets, showed no correlation between temperature and drift. Data was considered invalid for drift greater than  $\pm$  the standard error on the lower and upper energy bounds.

### 3.3 Optimisation of Acquisition times

The source used was 3.51MBq on date of commission, in Sept. 1995. Due to the relatively short half-life of the source ( $\approx 2.5$  yrs [6]) concern was raised over the time required for sufficient data at a given detector separation angle. Three sources of background were considered, those being:

- Uncorrelated source related events,  $R_{Bs}$
- Uncorrelated background events,  $R_{Bu}$
- Correlated background events,  $R_{Bc}$

These were considered to be constant for all detector separation angles. By taking a measurement of coincidences with the source present, and the relative delay of the system moved outside the coincidence resolution we obtain  $R_{Bs+Bu} = R_{Bs} + R_{Bu}$ . Similarly  $R_{Bc+Bu}$  may be obtained from prompt coincidences measured in the absence of the source, and  $R_{Bu}$  from delayed coincidences in the absence of the source.  $R_B = R_{Bs+Bc+Bu} = R_{Bs+Bu} + R_{Bc+Bu} - R_{Bu}$  is the total background, and must be accounted for in data analysis.

Preliminary data was captured at detector angular separation  $\psi = 0$  radians, and a measurement of  $R_{Bs+Bu}$ . Based upon rates at these configurations, and the assumption that  $R_{Bc} \ll R_{Bs+Bu}$  optimal counting times for each angle were modelled. For further details please refer to Appendix D.

### 3.4 Error minimisation

In order to avoid propagation of systematic errors, rather than deriving the relative intensity values directly from the experimental data the final models discussed in Appendix B.2 were modified to provide expected *rates* rather than intensities, based upon the rate  $R_S(\psi = 0)$  and the total background  $R_B$ . Upper and lower model bounds were calculated based upon the error in these parameters, which are dependent and therefore additive. A fit to the data would therefore be constrained by the bounds on the models, and provide an estimation of the actual values of  $R_S(\psi = 0)$  and  $R_B$ .

## 4 Results

Derived values of the coincidence rates for both models based upon  $R_B$  and  $R_S$  were determined to be:

$$R_{Quantum} = 0.50(7) \times 10^{-2} - 0.12(2) \times 10^{-2} \cos^2(\psi) \quad (14)$$

$$R_{local} = 0.43(6) \times 10^{-2} - 0.49(9) \times 10^{-3} \cos^2(\psi) \quad (15)$$

Where  $(\sigma)$  is the systematic error on the parameters  $\alpha, \beta$ .

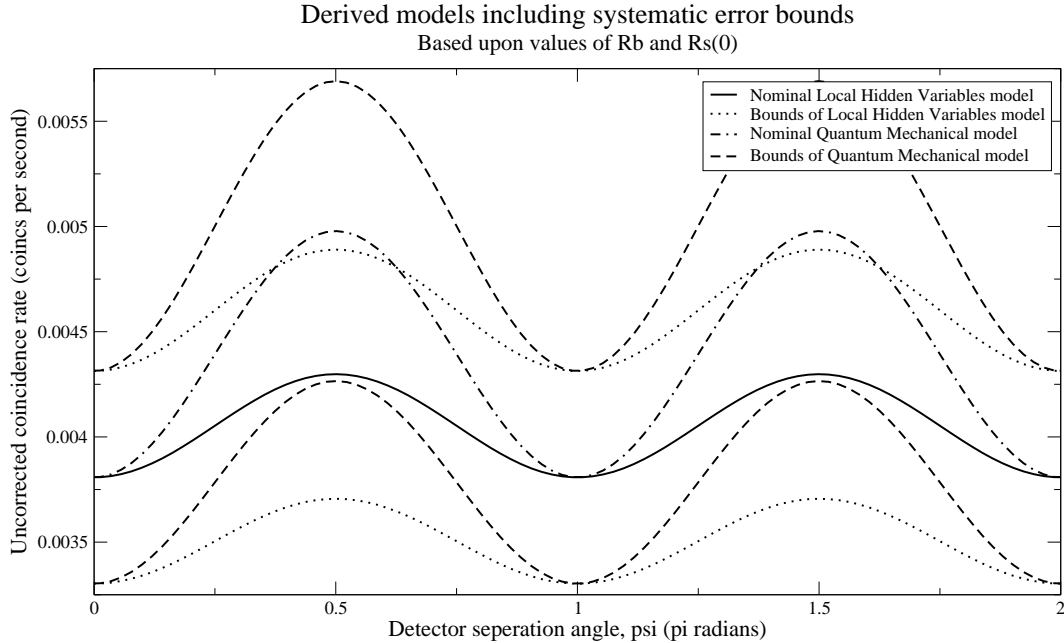


Figure 3: A plot of the models based upon background and the rate at 0 angular separation. Included are the lower and upper systematic error bounds for each model.

Data was initially acquired for the range  $0 \rightarrow \frac{\pi}{2}$  radians to ensure that the above models sufficiently specified the experimental apparatus. Based upon the goodness of fit of this data to the quantum model, further data was taken in the range  $\frac{\pi}{2} \rightarrow 2\pi$  to test for asymmetry. Throughout the course of the experiment measured drift was considered sufficiently small to accept all recorded data points. Data acquired at detector separation angles  $\frac{3\pi}{2}$  and  $\frac{7\pi}{4}$  were rejected however, as a mistake in the process of drift recalibration altered the gain on one detector to well outside the acceptable criteria. These were retaken at a later date. The measurement at 0 radians was taken over twice the approximated optimal counting rate in order to minimise the upper and lower bounds on the models. Measured values may be found in fig. 4

A Chi Squared goodness-of-fit calculation[7] was performed on the data with respect to the *nominal* values of both models, Providing reduced Chi Squared values of  $\chi_{Quantum}^2 = 0.75$ ,  $\chi_{local}^2 = 2.66$  With 2 constraints and therefore 8 degrees of freedom. A Fit to the data yields the function:

$$R_{fit} = 0.494(7) \times 10^{-2} - 0.12(1) \times 10^{-2} \cos^2(\psi) \quad (16)$$

$\psi$	$R_{S+B}$	$\sigma R_{S+B}$
0	0.00381	0.00012
$\frac{\pi}{4}$	0.00422	0.00018
$\frac{\pi}{3}$	0.00478	0.00019
$\frac{5\pi}{12}$	0.00502	0.00019
$\frac{\pi}{2}$	0.00511	0.00019
$\frac{3\pi}{4}$	0.00428	0.00018
$\pi$	0.00376	0.00017
$\frac{5\pi}{4}$	0.00422	0.00018
$\frac{3\pi}{2}$	0.00472	0.00018
$\frac{7\pi}{4}$	0.00428	0.00018
	$R_B$	$\sigma R_B$
$R_{Bs+Bu}$	0.00158	0.00014
$R_{Bc+Bu}$	0.00181	0.00015
$R_{Bu}$	0.00109	0.00012

Figure 4: Table of measured values of the Coincidence rate per second ( $R_{S+B}$ ) including associated errors, and background rates  $R_{Bs+Bu}$ ,  $R_{Bc+Bu}$ ,  $R_{Bu}$

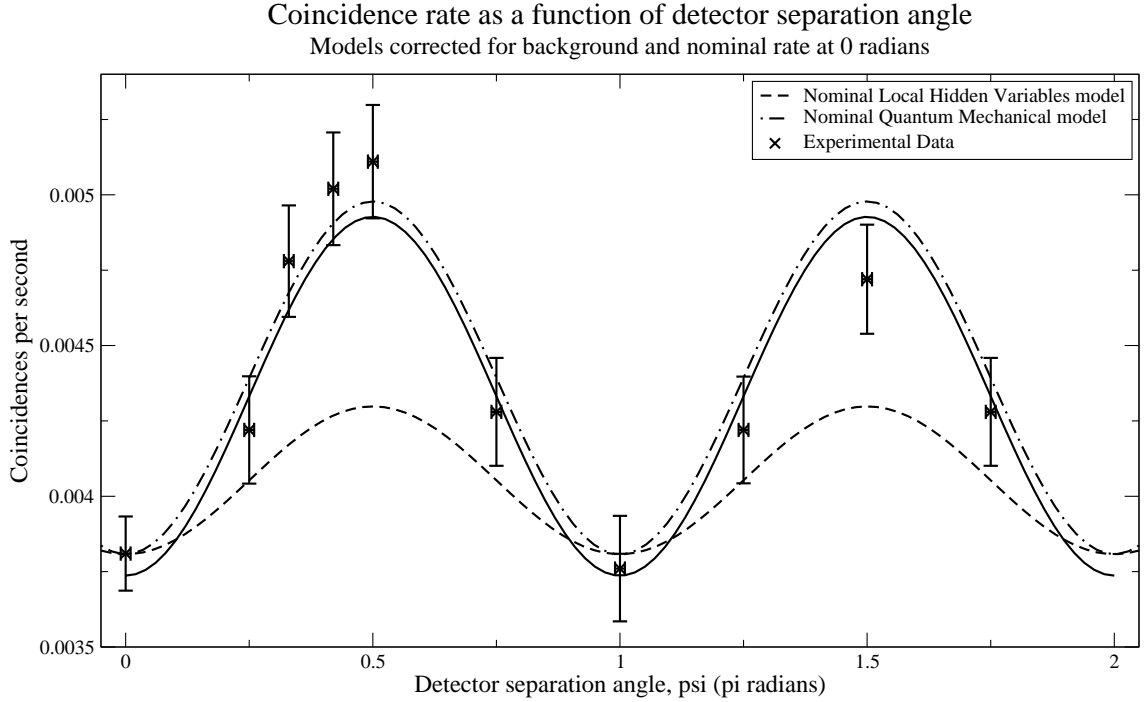


Figure 5: A plot of the coincidence rate variation with respect to detector separation angle. Also shown are the nominal quantum and hidden variables models, and a fit to the experimental data. Minor asymmetry exists between measurements at the same relative angular separation, but as predicted this was well within errors.

The  $\beta$  value of  $-0.12(1) \times 10^{-2}$  is over 6 standard errors outwith the upper limit imposed upon the hidden variables model of  $\beta = -0.58 \times 10^{-3}$  by systematic errors, but is in good agreement with the nominal quantum model. We may therefore assume that the data is in good agreement with the nominal values of the measured background rate and coincidence rate at 0 radians. the Chi Squared values with respect to the nominal models provide *highly significant* disagreement with the hidden variables model at the 1% level and acceptance of the Quantum model at the 60% level.

## 5 Conclusion

The experimental results show good agreement with the quantum-mechanical model, providing clear violation of the principle of locality for quantum-mechanical processes. Improvements could be made by reducing  $d\phi$  and  $d\delta$ ; It was noted during the modelling process that the Quantum Mechanical and Local Hidden Variables models became increasingly convergent as the detectable range of scattering and polarisation angles increased. Reduction in detector size and scatterer volume would reduce these ranges, further limiting the ambiguity between the models at the expense of reduced coincidence rates. Further minimisation of systematic errors would require a stronger source and as a result, longer optimised background counting times. These in turn would minimise the bounds on both models and provide a more conclusive fit. The asymmetry noticed in figure 4 would also be worthy of further investigation; due to time constraints fewer measurements were taken between  $\pi \rightarrow 2\pi$  radians than from  $0 \rightarrow \pi$ , and the second detector was not rotated. By taking further measurements expectation values would provide more conclusive data.

It is important to note however that regardless of the above considerations the experiment does not fully satisfy the requirements imposed upon a Bell Test Experiment, and therefore cannot completely rule out a local hidden variables theory. In order to satisfy a Bell Inequality of the simplest type commonly referred to as the CHSH[8] inequality “perfect” or near-perfect half-wave plate polarisers are required that function at  $\gamma$  energies. This allows for coincidence measurements at each relative polariser angle in the absence of none, one or both polarisers, yielding the inequality:

$$S = \frac{N(a, b) - N(a, b') + N(a', b) + N(a', b') - N(a', \infty) - N(\infty, b)}{N(\infty, \infty)} \quad -1 \leq S \leq 0 \quad (17)$$

where  $a, b, a', b'$  are two particular polariser orientations of detectors  $A$  and  $B$ ,  $N$  is the coincidence rate measured in this configuration and  $\infty$  is a measurement performed with that particular polariser removed.

Further work has been performed in altering these inequalities to better suit actual experimental configurations, in particular the substitution of expectation values rather than counting rates for opposing relative angular separations of the detectors in order to account for asymmetries in the apparatus.

If we assume however, that results provided by compton polarimetry are in good quantum-mechanical agreement with those of a perfect linear polariser, we can arrange an experiment of the type implemented by Kasday, Ullman & Wu[5] with only minor

modification to the current apparatus. This allows for measurement of  $N(\infty)$  by replacing perspex scatterers with another pair of scintillator crystals mounted on PMTs. A four-fold coincidence technique is now employed, where the energy deposited in the scatterer by compton scattering is measured. Three-fold coincidences provide  $N(a', \infty)$  and  $N(\infty, b)$ , Two-fold  $N(\infty, \infty)$  and Four-fold all other necessary values. There is a much greater reliance on this type of experiment for full specification of scattering processes, due to the reliance upon accurate measurement of both detected and undetected events. Our experiment does not need to take into account double scattering events in the scatterer as these remain undetected and do not contribute to the model.

A measurement of this type would confirm violation of the Principle of Locality and therefore rule out any local hidden variables theory. Even this, however, is insufficient to confirm that quantum mechanics is the only complete solution to the phenomena it is associated with<sup>3</sup>. A number of experiments have been performed by others[8] that further investigate Bell's Inequalities, yielding more conclusive results.

---

<sup>3</sup>It is the author's opinion that the application of *occham's razor* is suitable here. Many of the theories proposed as replacements to quantum mechanics that provide similar predictions of violation of the inequalities as yet fail to fully specify a number of phenomena that agree with quantum-mechanical calculations, or become needlessly complex in order to do so.

## 6 Appendices

## A Compton Polarimetry

The annihilation photons are of energy  $m_e c^2 = 511keV$ [6]. Efficient half-wave plate polarisers at these energies do not exist, and as such other methods of measurement are required. Compton Polarimetry[9] is a well understood technique for such measurements, but is only applicable to linearly polarised light. An incident photon scatters off an electron elastically, imparting energy to the electron. The scattering angle defines this energy loss, but of more interest is the polarisation relationship. We consider the Klein-Nishina differential cross-section for compton scattering:

$$\frac{d\sigma}{d\Omega} = \frac{1}{2}r_0^2 \frac{\frac{k}{k_0} + \frac{k_0}{k} - 2\sin^2(\delta)\cos^2(\phi)}{k_0^2} \quad (18)$$

Where  $r_0$  is the classical electron radius,  $k$  is the scattered photon energy,  $k_0$  the incident photon energy,  $\delta$  is the compton scattering angle and  $\phi$  is the polarisation orientation with respect to the detector, which we initially consider to be  $\phi \rightarrow 0$ .

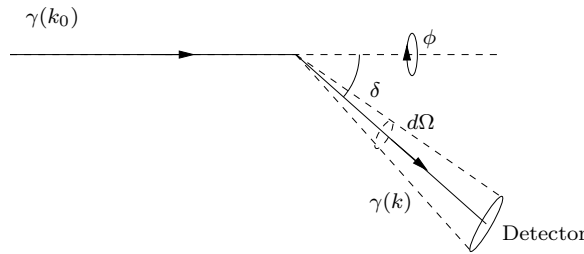


Figure 6: The differential cross-section for elastic compton scattering of a photon incident upon an electron.

Conveniently, a simplification of the Klein-Nishina formula arises from the incident photon energy. We appeal to the compton scattering formula:

$$k = \frac{k_0}{1 + \left(\frac{k_0}{m_e c^2}\right) (1 - \cos(\delta))} \quad (19)$$

Substituting for our incident photon energy,  $k_0 = m_e c^2$ :

$$k = \frac{m_e c^2}{2 - \cos(\delta)} \quad (20)$$

And in turn substituting this into  $\frac{d\sigma}{d\Omega}$  yields the result:

$$\frac{d\sigma}{d\Omega} = \frac{1}{2}r_0^2 \frac{\frac{1}{2-\cos(\delta)} + 2 - \cos(\delta) - 2\sin^2(\delta)\cos^2(\phi)}{2 - \cos^2(\delta)} \quad (21)$$

This is purely a function of  $\phi$  and  $\delta$ , which parameterise  $d\Omega$  The scattered intensity relative to the incident flux is therefore

$$I = \int_{\phi_{min}}^{\phi_{max}} \int_{\delta_{min}}^{\delta_{max}} \frac{d\sigma}{d\Omega} d\delta d\phi \quad (22)$$

## B modelling

Geometric modelling of the experimental apparatus was performed using numeric integration techniques. We first consider the simplest application of the Klein-Nishina formula, scattering of an infinitesimal beam by a point into a pointlike detector, as shown in figure 7:

### B.1 Simple model and derivation of relative intensities

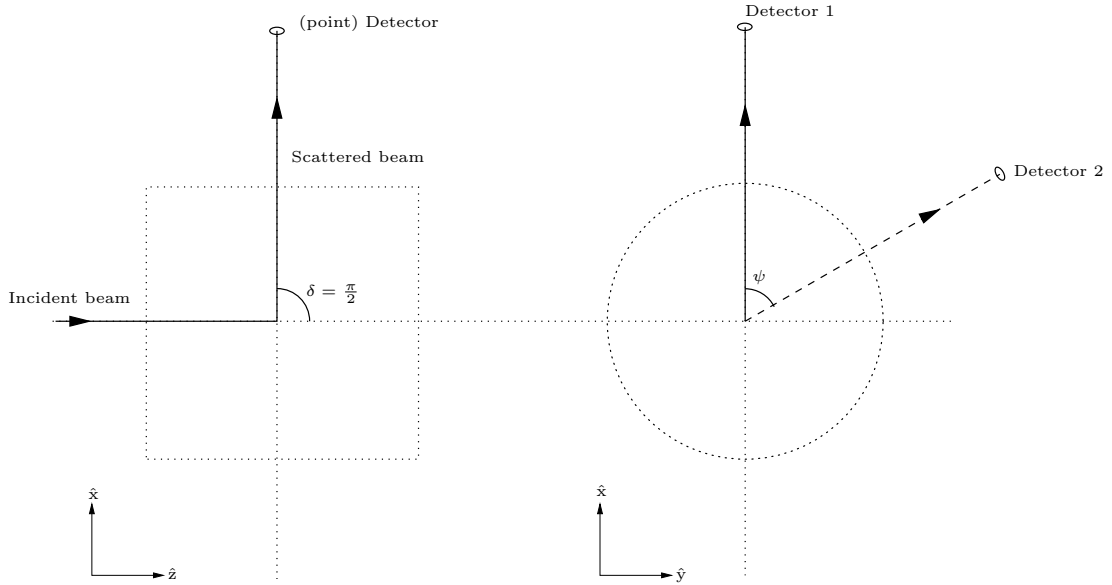


Figure 7: The initial model. An infinitely thin beam of  $\gamma$ s incident upon a point-like scatterer centered within the actual scatterer. The scattered beam is then incident upon a point detector.

#### B.1.1 Quantum model

Let us first consider the quantum wavefunction, with a photon incident upon the first polarimeter. Applying this model to eq. 21, we note:

$$\frac{d\sigma}{d\Omega} \left( \delta = \frac{\pi}{2} \right) = \frac{1}{8} r_0^2 \left( \frac{5}{2} - 2\cos^2(\phi) \right) \quad (23)$$

We consider two constants of proportionality,  $\alpha$  and  $\beta$  such that:

$$\frac{d\sigma}{d\Omega} = \alpha + \beta \cos^2(\phi) \quad (24)$$

Solving with respect to this model for  $\alpha$ ,  $\beta$  yields:

$$\alpha = \frac{d\sigma}{d\Omega} \left( \phi = \frac{\pi}{2} \right) = \frac{5}{16} r_0^2 \quad (25)$$

$$\beta = \frac{d\sigma}{d\Omega}(\phi = 0) - \alpha = -\frac{1}{4}r_0^2 \quad (26)$$

For the state  $|x_1\rangle$ , this component of  $\sigma$  is:

$$\frac{d\sigma}{d\Omega_{|x_1\rangle}} = \frac{d\sigma}{d\Omega}(\phi = 0) = \alpha + \beta \quad (27)$$

and similarly for  $|y_1\rangle$ :

$$\frac{d\sigma}{d\Omega_{|y_1\rangle}} = \frac{d\sigma}{d\Omega}(\phi = \frac{\pi}{2}) = \alpha \quad (28)$$

We now turn to the second detector, at an angle  $\psi$  with respect to the first.

$$\frac{d\sigma}{d\Omega_{|x_2\rangle}} = \alpha + \beta \cos^2(\psi) \quad (29)$$

for  $|y_2\rangle$ :

$$\frac{d\sigma}{d\Omega_{|y_2\rangle}} = \alpha + \beta \sin^2(\psi) \quad (30)$$

Now,  $\langle x_1|\Psi\rangle = i|y_2\rangle$ , and  $\langle y_1|\Psi\rangle = i|x_2\rangle$ . The intensity is therefore:

$$I_{Quantum}(\psi) = (\alpha + \beta)(\alpha + \beta \sin^2(\psi)) + \alpha(\alpha + \beta \cos^2(\psi)) \quad (31)$$

$$\Rightarrow I_{Quantum}(\psi) = 2\alpha^2 + 2\alpha\beta + \beta^2 - \beta^2 \cos^2(\psi) \quad (32)$$

### B.1.2 Local Hidden Variables Model

By similar argument, the detector response with respect to polarisation orientation at the first detector is:

$$\frac{d\sigma}{d\Omega_{|\Psi_1\rangle}} = \alpha + \beta \cos^2(\phi) \quad (33)$$

Contrary to the quantum-mechanical formulation, the response at the second detector is not dependent upon the response at the first:

$$\frac{d\sigma}{d\Omega_{|\Psi_2\rangle}} = \alpha + \beta \cos^2\left(\phi + \frac{\pi}{2} - \psi\right) \quad (34)$$

The overall intensity being the product of these functions. Calculating the average given that  $\phi$  is randomly distributed:

$$I_{local}(\psi) = \frac{1}{2\pi} \int_0^{2\pi} (\alpha + \beta \cos^2(\phi)) \left( \alpha + \beta \cos^2\left(\phi + \frac{\pi}{2} - \psi\right) \right) d\phi \quad (35)$$

$$\Rightarrow I_{local}(\psi) = \left( \alpha^2 + \frac{\beta^2}{8} + \alpha\beta \right) + \frac{\beta^2}{4} \sin^2(\psi) \quad (36)$$

The relative intensity at a given detector separation angle is calculated with respect to  $I(\psi = 0)$ :

$$I_{Rel}(\psi) = \frac{I(\psi)}{I(0)} \quad (37)$$

## B.2 Further modelling

The previous model does not specify the experimental apparatus sufficiently. In order to obtain a meaningful fit to experimental data, further models were investigated. Based upon the incident beam geometry the final model shown in fig 8 describes the scatterer as a conical frustum, and the detector as a disc.

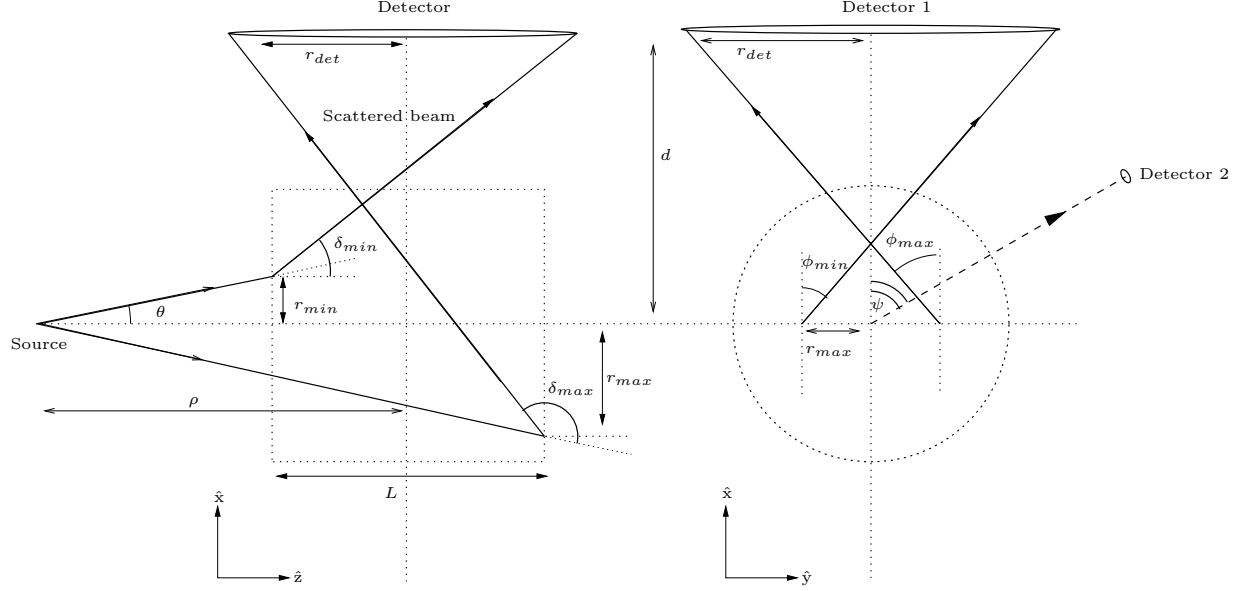


Figure 8: The final model. A collimated beam of  $\gamma$ s incident upon a cylindrical scatterer, centred upon a disc detector. The incident beam does not intersect with the entire scatterer, and so this was modelled as a conical frustum. The differential cross-section was integrated over the range of compton angles and polarisation angles that could be detected by the apparatus based upon this geometry.

The maximum and minimum values of  $\delta$  and  $\phi$  were obtained in terms of the dimensions of the scatterer and detector as follows:

### B.2.1 Compton angle specification

The incident beam diverges from the collimator at angle  $\theta$ , as defined by the source-collimator distance and collimator radius:

$$\theta = \tan^{-1} \left( \frac{r_{col}}{l_{col}} \right) \quad (38)$$

The maximum and minimum radial deviation from the centre of the scatterer is therefore:

$$r_{max} = \left( \rho + \frac{L}{2} \right) \tan(\theta) = \left( \rho + \frac{L}{2} \right) \frac{r_{col}}{l_{col}} \quad (39)$$

$$r_{min} = \left( \rho - \frac{L}{2} \right) \tan(\theta) = \left( \rho - \frac{L}{2} \right) \frac{r_{col}}{l_{col}} \quad (40)$$

The minimum angle at which photons scatter and may still be detected occurs from the front of the scatterer into the back of the detector:

$$\delta_{min} = \tan^{-1} \left( \frac{d - r_{min}}{r_{det} + \frac{L}{2}} \right) - \theta \quad (41)$$

Similarly, the maximum detected compton angle occurs for photons scattered at the back of the scatterer into the front of the detector:

$$\delta_{max} = \tan^{-1} \left( \frac{r_{det} + \frac{L}{2}}{d + r_{max}} \right) + \theta + \frac{\pi}{2} \quad (42)$$

### B.2.2 Polarisation angle specification

The range of polarisation angles relative to the detector orientation is symmetric assuming the scatterer is centred upon the detector, and maximum at the back of the scatterer:

$$\phi_{max} = \tan^{-1} \left( \frac{r_{det} + r_{max}}{d} \right) \quad \phi_{min} = -\phi_{max} \quad (43)$$

With  $d = 15cm$ ,  $\rho = 50cm$ ,  $L = 7.5cm$ ,  $r_{det} = 3.56cm$ ,  $r_{col} = 0.5cm$ ,  $l_{col} = 10cm$ , we find:

$$I = \int_{\phi_{min}}^{\phi_{max}} \int_{\delta_{min}}^{\delta_{max}} \frac{d\sigma}{d\Omega} d\delta d\phi = \int_{-0.4087}^{0.4087} \int_{0.9702}^{2.0247} \frac{d\sigma}{d\Omega} d\delta d\Omega \quad (44)$$

$$\Rightarrow 0.2861r_0^2 - 0.1978r_0^2 \cos^2(\psi) \quad (4d.p.) \quad (45)$$

Solving for  $\alpha$ ,  $\beta$  is trivial. Applying these to eq. 32 and eq. 36, then normalising wrt  $I(0)$  yields the relative intensity functions:

$$I_{Quantum}(\psi) = 1.7748 - 0.7748 \cos^2(\psi) \quad (46)$$

$$I_{local}(\psi) = 1.3246 - 0.3246 \cos^2(\psi) \quad (47)$$

These are the final relative intensity functions considered in the report.

## C Detector Calibration & Configuration

A standard two-fold coincidence configuration was used, consisting of readily available NIM components. Care was taken to ensure that at every stage of the initial calibration and final data acquisition stages the signal path was unaltered due to the timing delay and impedance properties of each component. To capture spectral data, an Ortec Trump PCI MCB[10] card was used. In order to determine energy window requirements, the energy per MCB channel for both detector systems needed to be well known.

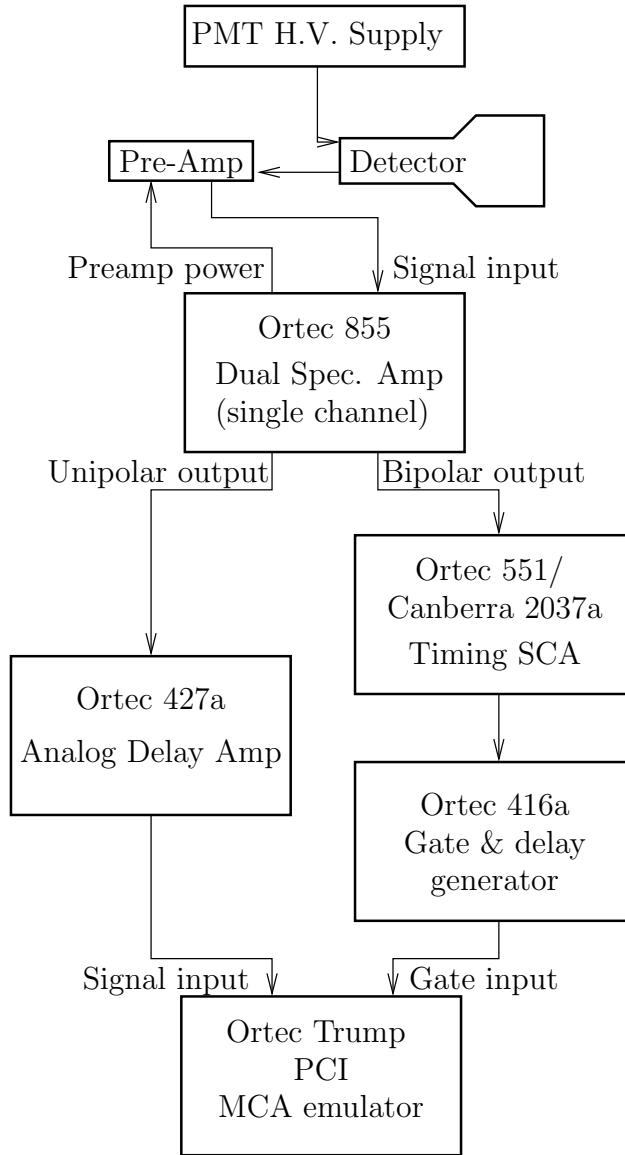


Figure 9: NIM configuration used to determine the detector resolution and eV per channel.

## C.1 Channel-Energy determination

The configuration shown in fig.9 was used identically for both detectors. The MCB is a 2048 channel system, designed to be used with Germanium based detectors, which have a considerably higher energy resolution. As such, the gain on both spectroscopy amplifiers was initially altered by-eye to provide sub-2keV/channel resolution, better suited to NaI(Tl) type detectors. All variable delays were set to their minimum values, and ungated spectra were captured for 55 minutes for a range of available calibration sources on each detector. Background rates were captured for the same length of time, with no consideration for optimisation of counting times. The MCB features on-board deadtime correction and given the source intensities the dead time of the photomultiplier

detectors were considered insignificant.

Calibration sources used were:  $^{22}\text{Na}$ ,  $^{137}\text{Cs}$  and  $^{60}\text{Co}$ , providing 5 emission peaks. These spectra were background corrected, and were fitted to gaussians, whose mean and standard error were then used to generate a linear fit. Concern was noted that no calibration source was available in the range of interest for scattered 511keV photons, but the linearity as noted in the MCB specifications, combined with the goodness of the linear fit allayed any such concerns.

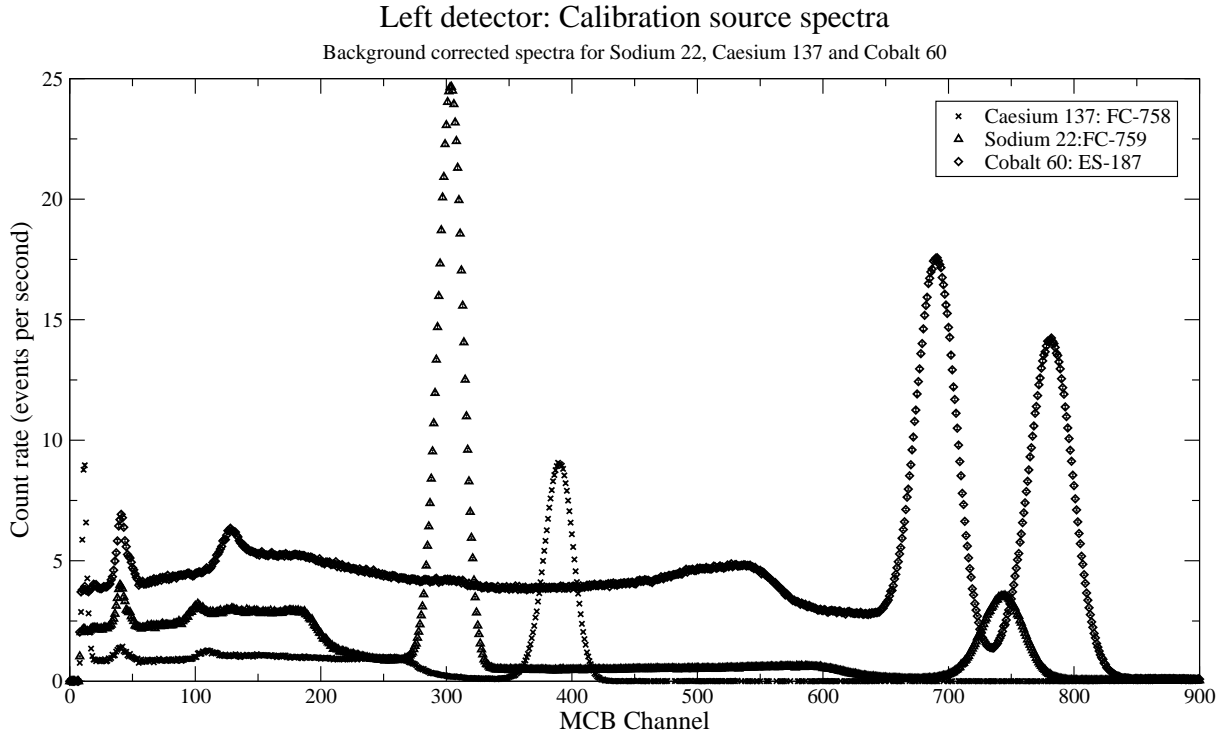


Figure 10: Spectra of all three calibration sources captured for the left detector. Error bars are too small to be distinguished. The peaks are, in order of increasing energy, 511keV, 662keV, 1173keV, 1275keV and 1333keV respectively.

In order for this fit to remain valid, regular drift checks were performed using the same  $^{22}\text{Na}$  source. This source was chosen as the 511keV and 1275keV peaks were sufficiently separated to detect both bias drift and gain drift. The spectroscopy amplifier gain was adjusted until both of these peaks fell within errors of their fitted values. Throughout the course of the experiment, bias drift was never witnessed.

## C.2 Timing calibration

The system was now configured for two-fold coincidence counting as shown in fig.12. As timing is critical to the coincidence requirement, efforts were made to ensure the maximum possible time resolution of the system was used[11]. This was achieved by ensuring bipolar outputs were used in the coincidence path wherever possible. Unipolar outputs were used for diagnostic purposes.

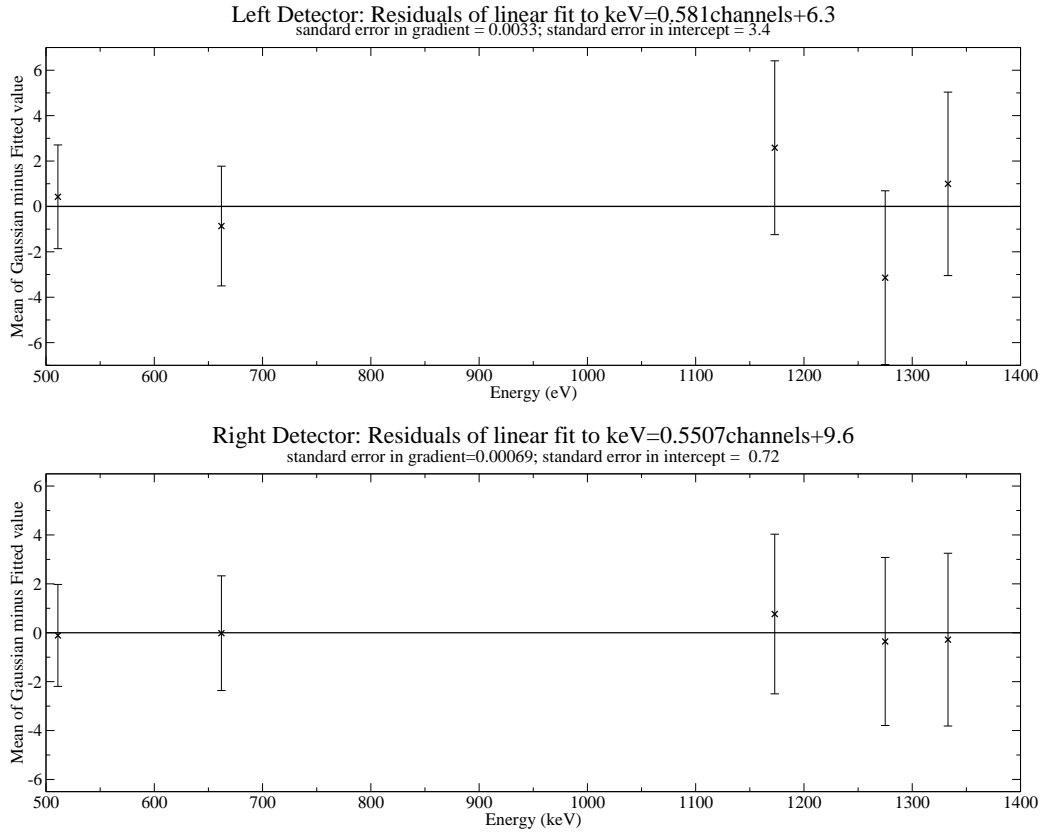


Figure 11: Linear fits of the gaussian means of the spectral peaks captured for both detectors. Note that in both cases errors were overestimated, but particularly so in the case of the right detector. This was in part due to underestimation of the resolution of the detectors, and due to the propagation of systematic errors due to the background measurement

To minimise the effect of random coincidence events the coincidence resolving time was minimised by making use of the pulse regeneration system available on the 418A Universal Coincidence unit[12]. the unipolar input to channel “A” on this unit may be regenerated with a gate width variable from 100ns to  $2\mu\text{s}$ , with other channels accepting standard 500ns gate widths, providing a combined variable timing resolution of  $600\text{ns} \rightarrow 2500\text{ns}$ . By taking into consideration the maximum path-length difference of two coincidental photons emitted from the source, and possible pulse generation time variations in the electronics, it was decided that the minimum possible coincidence resolving time would still be larger than needed to ensure all truly coincidental events were recorded. The “A” input relies heavily upon the characteristics of the input signal, and as such requires careful impedance matching. Standard  $50\Omega$  BNC cable was employed as signal carrier, and so a  $50\Omega$  terminator was employed at the input. Finite timing differences in the electronics needed to be accounted for in order to ensure optimal coincidence rates. The Ortec 551 SCA units[13] were used in “window” mode, with the lower level and window set to  $\pm 3\sigma$  of the 511keV peak based upon the channel values calculated in section C.1. Both detectors were positioned diametrically opposite the  $^{22}\text{Na}$  source. By varying the

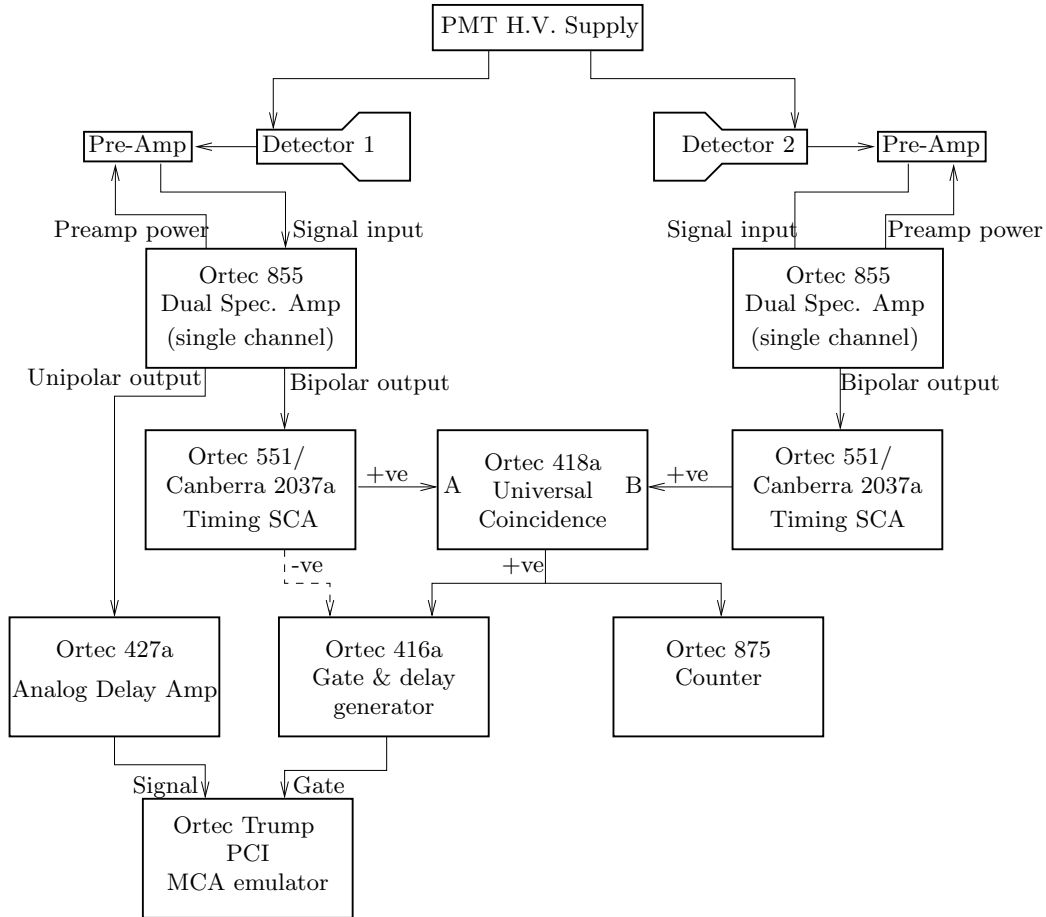


Figure 12: NIM configuration used to detect coincidental  $\gamma$ s.

delay on one SCA with respect to the other, the relative delay of the signal paths could be determined, in addition to actual coincidence resolution time. Initial measurements proved inconsistent, and it was determined that the delay potentiometer on the SCA associated with the left detector was malfunctioning. This was replaced with a similar unit produced by Canberra[14].

The optimal relative delay was calculated from the mean of the upper values of figure 13, and was determined to be 50ns. This was applied to the right detector. The half maximal full width of the same data gives a measure of the coincidence resolution time, in this case  $0.549\mu\text{s}$ .

### C.3 Energy coincidence criteria

The energy range to which the SCAs were set to trigger on was initially based upon the geometry of the scatterer as defined in section B. This provided the theoretical maximum and minimum Compton angles, which when applied to eq 19 provided absolute maximum and minimum expected coincidental energies. These were converted to channel ranges with respect to each detector, allowing the SCA windows to be set by eye using the MCB during a realtime capture. Preliminary coincidence gated spectra at 0 and  $\frac{\pi}{2}$  radians

showed a poor signal to noise ratio after the exclusion of source-related background. Additional coincidence gated spectra were captured over an energy range approximately twice that of the original values, the concern being that the model did not completely specify the system. These spectra were corrected for background, and a difference taken as show in figure 14. Further modelling was deemed necessary in order to confirm the region of suspected signal.

The apparent optimal signal region in figure 14 corresponds to energies  $202(6)\text{keV} \rightarrow 282(6)\text{keV}$ . This was within the proposed range of  $199\text{keV} \rightarrow 354\text{keV}$ , but significantly narrower and lower. It was proposed that beam attenuation within the perspex scatterer should be investigated. Similarly, the variation in compton angle with respect to scatterer penetration depth was investigated.

Figure 15 Shows that the maximum beam attenuation is a little below 50%. Of far greater interest is the effect penetration depth has upon the scattered photon energy. The second graph shows the maximum and minimum compton scattering energy as a function of penetration depth based on the minimum and maximum scattering angles for which a photon still interacts with the detector. The contribution to the energy spectrum converges upon the range  $200 \rightarrow 270 \text{ keV}$  as the penetration depth increases. Contributions to the energy spectrum at shorter depths are spread over a wider range than those further into the scatterer. If we sum the contributions to the energy spectrum at all depths, we expect that the maximum signal will be present in the  $255\text{-}270\text{keV}$  range, with a bias towards the  $200\text{-}280\text{keV}$  range. Even with the inclusion of beam attenuation we note that this still favors lower energy ranges, providing excellent agreement with figure 14.

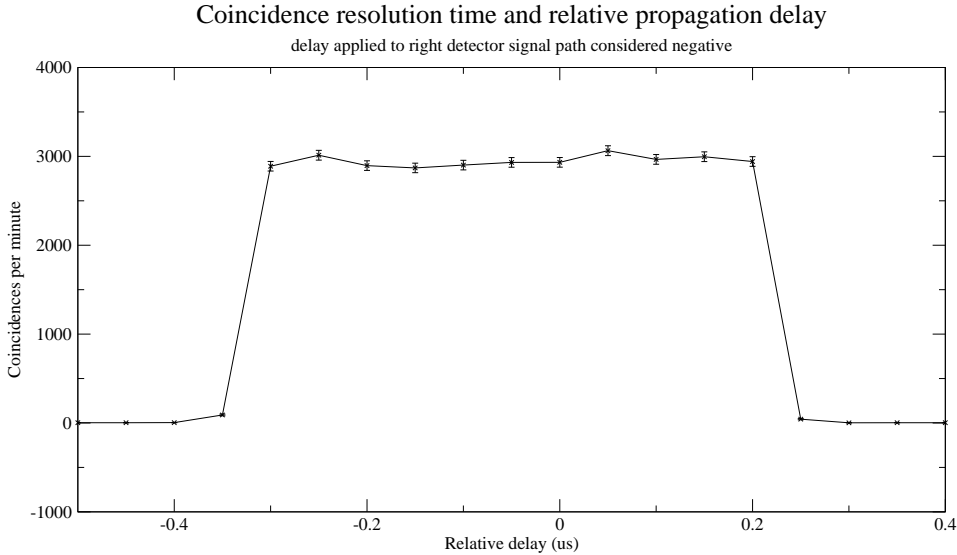


Figure 13: Timing resolution graph produced by variation of SCA delay, whilst detecting coincidental  $511\text{keV}$   $\gamma$ s. The mean x value of the upper region gives optimal delay with respect to the left detector, and the full width at half maximum gives the coincidence timing resolution of the system.

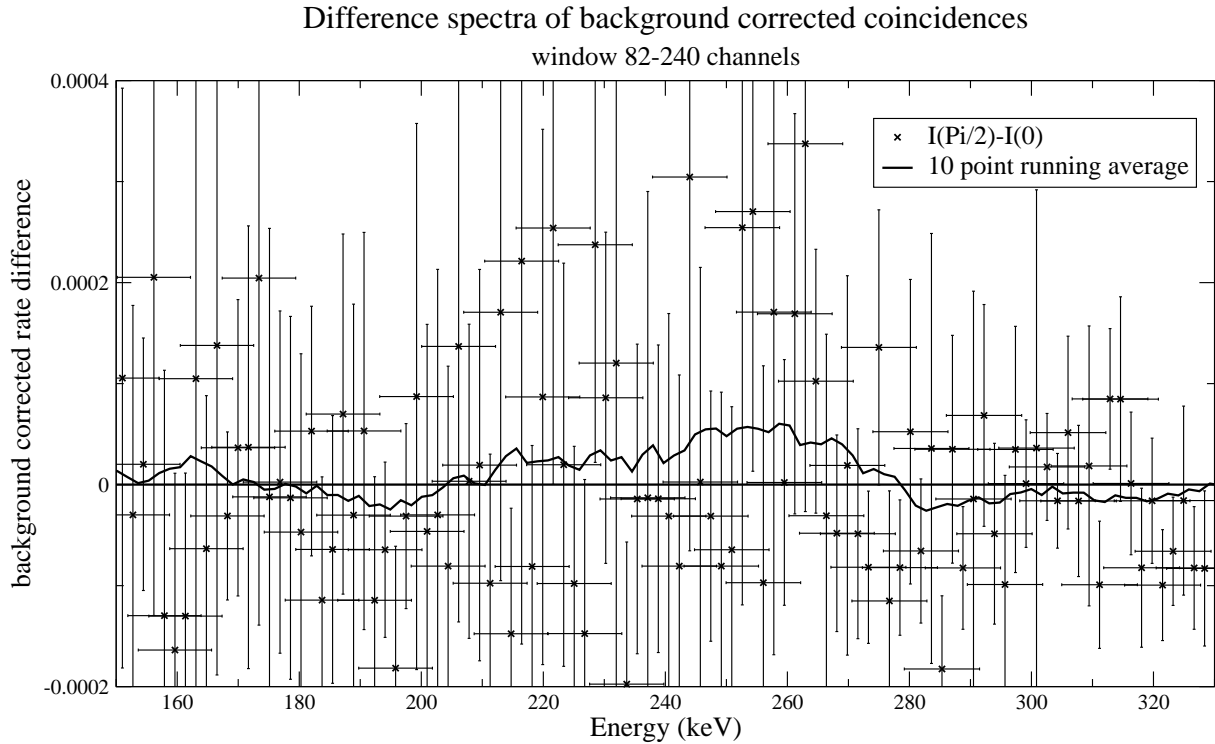


Figure 14: The difference of background corrected coincidence spectra acquired at 0 and  $\frac{\pi}{2}$  radians (Left detector spectra displayed). A 10-point running average suggests that maximum difference occurs in the region 120-170 channels (200-280keV)

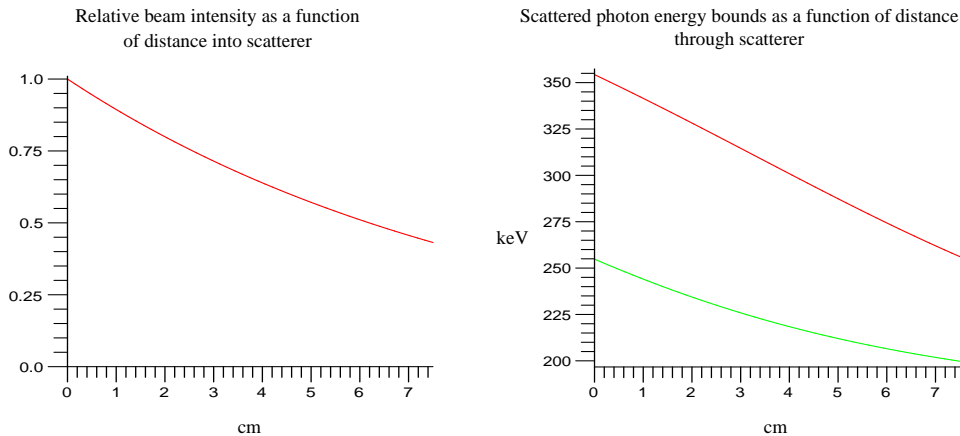


Figure 15: Plots of beam attenuation and expected scattered photon energy ranges with respect to scatterer penetration depth

## D Error and acquisition time optimisation

The error in the rate of a decay event is subject to poisson statistics,  $\sigma_N = \sqrt{N}$ . In order to minimise the error on a given measurement, long acquisition times may be used, but

this is impractical. In order to optimise the acquisition time at a given detector angle, we considered the following equation[15]:

$$\frac{T_{S+B}}{T_B} = \sqrt{\frac{R_{S+B}}{R_B}} \quad (48)$$

where T is the optimal acquisition time, R the detected rate, S the source contribution, and B the background contribution. Approximate rates  $R_{S+B}$  and  $R_{B_s+B_u}$  were obtained from preliminary measurements of the prompt coincidence rate at 0 radians and the delayed coincidence rate at 0 radians respectively. The background rate neglected to account for prompt background coincidences as this would require removal of the source and realignment of the apparatus, but it was assumed that the prompt background coincidence rate was sufficiently small that it would have minimal impact upon optimisation times. Assuming that the background rate was constant for all angles, only one measurement of each background component was deemed necessary. Assuming the final model derived in section B specified the relative intensities at every angle sufficiently, optimal acquisition times were calculated as follows:

$$T_{S+B}(\psi) = T_B \sqrt{\frac{R_S(\psi = 0)I_{Rel}(\psi) + R_B}{R_B}} \quad (49)$$

Where  $R_S(\psi = 0)$  is the background-corrected source rate at 0 radians. The minimum background capture time was calculated that would provide errors small enough to prevent ambiguity between the two models at a given minimum angle. 22hrs was considered sufficient to provide a measurement just preventing ambiguity at  $\psi = \frac{\pi}{6}$ . The maximum and minimum acquisition times were calculated to be 34 hours at  $\psi = 0, \pi$  and 40 hours at  $\psi = \frac{\pi}{2}, \frac{3\pi}{2}$ .

## References

- [1] A. Einstein, B. Podolski, and N. Rosen, Phys. Rev. **47**, 777 (1935), *Can Quantum-Mechanical Description of Physical Reality Be Considered Complete?*
- [2] J. S. Bell, Physics **1**, 195 (1964), *On the Einstein Podolski Rosen Paradox*.
- [3] *Photomultiplier Tubes; Basics and Applications*, Second ed. (Hamamatsu Photonics K. K., 1999), chap. 3.5.1; Scintillators and Photomultiplier Tubes, pp. 86–100.
- [4] M. A. Coplan, J. H. Moore, and C. C. Davis, *Building Scientific Apparatus- A Practical Guide to Design and Construction*, Third ed. (Westview Press, 2003), chap. Optics; Detectors; Photomultipliers, pp. 304–317, ISBN 0-8133-4007-3.
- [5] L. R. Kasday, J. D. Ullman, and C. S. Wu, Il Nuovo Cimento Della Soc. Ital. Fisica B **B25**, 633 (1975), *Angular Correlation of Compton-Scattered Annihilation Photons and Hidden Variables*.
- [6] K. Hagiwara et al., *Particle Physics Booklet* (Particle Data Group, 2002), Extracted from the *Review of Particle Physics*, Phys. Rev. D66, 010001 (2002).
- [7] J. R. Taylor, *An Introduction to Error Analysis*, Second ed. (University Science Books, 1997), chap. 12.4- Probabilities for Chi Squared, ISBN 0-935702-75-X.
- [8] A. Aspect, J. Dalibard, and G. Roger, Phys. Rev. Lett. **49**, 1804 (1982), *Experimental Test of Bell's Inequalities Using Time-Varying Analyzers*.
- [9] H. Frauenfelder and R. M. Steffen, Alpha, Beta and Gamma Spectroscopy **2** (1965).
- [10] Ortec, Trump pci mca specification sheet, 2006, <http://www.ortec-online.com/pdf/trumppci.pdf>, [Online; accessed 4-March-2006].
- [11] M. A. Coplan, J. H. Moore, and C. C. Davis, *Building Scientific Apparatus- A Practical Guide to Design and Construction*, Third ed. (Westview Press, 2003), chap. Electronics; Amplifiers and Pulse Electronics; Detecting and Processing Pulses, pp. 465–472, ISBN 0-8133-4007-3.
- [12] Ortec, 418a universal coincidence specification sheet, 2002, <http://www.ortec-online.com/pdf/418A.pdf>, [Online; accessed 8-March-2006].
- [13] Ortec, 551 timing single channel analyzer specification sheet, 2006, <http://www.ortec-online.com/pdf/551.pdf>, [Online; accessed 7-November-2006].
- [14] Canberra, 2037a edge/crossover timing single channel analyzer specification sheet, 2006, [http://canberra.com/pdf/Products/NIM\\_pdf/3m2037.pdf](http://canberra.com/pdf/Products/NIM_pdf/3m2037.pdf), [Online; accessed 14-November-2006].
- [15] G. F. Knoll, *Radiation Detection and Measurement* (John Wiley And Sons, 1979), ISBN 0-471-49545-X.